

High Mobility Anisotropic Black Phosphorus Nanoribbon Field-Effect Transistor

Xuwei Feng, Xin Huang, Li Chen, Wee Chong Tan, Lin Wang, and Kah-Wee Ang*

Achieving excellent electrostatic control and immunity to short channel effects are the formidable challenges in ultrascaled devices. 3D device architectures, such as nanoribbon, have successfully mitigated these problems by achieving uniform top- and side-wall control of the channel. Here, by leveraging on the merits of 3D structure, high-mobility black phosphorus nanoribbon field-effect transistors (BPNR-FET) are demonstrated and the anisotropic transport properties are systematically investigated. A simple top-down reactive ion etching method is used to realize both armchair- and zigzag-oriented nanoribbons with various widths down to 60 nm. The mobility of BPNR-FET is found to be width- and thickness-dependent, with the highest hole mobility of $\approx 862 \text{ cm}^2 \text{ V}^{-1} \text{ s}^{-1}$ demonstrated in armchair-oriented device at room temperature by combining high- κ gate dielectric and hydrogen treatment to reduce sidewall scattering. Furthermore, hydrogenation effectively passivates the nanoribbon dangling bonds, leading to hysteresis and contact resistance improvement. This work unravels the superior electrical performance underscore a conceptually new device based on BP nanoribbons, paving the way toward the development of nonplanar devices on 2D materials platform.

1. Introduction

Black phosphorus has undergone a renaissance due to its successful mechanical exfoliation from bulk crystal since the synthesis by Bridgeman in 1914.^[1] Apart from graphene, it is by far the other known monotypic atomically thin 2D material. However, unlike gapless graphene, BP possesses tunable direct bandgap properties as a function of layer thickness from 2.0 eV for monolayer to 0.3 eV in bulk. The presence of direct bandgap enables the realization of BP transistors with excellent switching speed ($>10^5$) and ultrahigh hole field-effect mobility ($>1000 \text{ cm}^2 \text{ V}^{-1} \text{ s}^{-1}$),^[2–4] which bridges the gap in mobility and on-off ratio among graphene and 2D transition metal dichalcogenides (TMDs).^[5–7] Moreover, the wide bandgap tuning

range makes it feasible for broadband optical detection from the ultraviolet to the infrared wavelengths. Some early reports on BP photodetectors show its rich potential for optoelectronic applications^[8,9] while achieving compatibility with complex photonic structures such as silicon waveguide and metallic nanoplasmonics.^[10]


Shaping 2D materials into low-dimensional structures such as nanoribbons came into prominence as an ideal configuration for the investigation of dimensional-dependent fundamental properties and nanoscale application.^[11–14] For instance, graphene nanoribbons (GNRs) were extensively researched to open up bandgaps, achieve GNRs field effect transistor, and plasmonic detection.^[12–14] To date, numerous theoretical predictions on the electronic structures and charge mobilities of BP nanoribbons have been reported.^[15,16] A flexible tunability in carrier mobility and bandgap is predicted.

Another advantage of BP beyond graphene is the strong intrinsic in-plane anisotropy along the light (armchair) and heavy (zigzag) effective mass direction as evidenced by the anisotropic optical conductivity and DC conductance.^[7,17,18] The realization of a 200 nm wide nanoribbon structure provides a platform for the study of anisotropic in-plane thermal transport in BP, which shed light on thermal conductivity and phonon physics.^[19] It was also predicted that the inherent anisotropy enables BPNR to display polarization-dependent plasmonic response in mid-infrared and far-infrared wavelength regime.^[20] In one pioneering study, lithography technologies have been developed to sculpture single BP nanoribbon,^[21] but large areas periodic nanoribbons arrays are required for collective plasmonic excitations. Furthermore, the electrical properties of BP nanoribbons FET have yet to be reported due to the lack of experimental demonstration.

Here, we report on high-performance anisotropic black phosphorus nanoribbons field-effect transistor (BPNR-FET) via reactive ion etching (RIE) method. The top-down RIE process enables accurate positioning of BPNR and a precise control of BPNR width down to 60 nm. The orientation-dependent study demonstrates that armchair is a more favorable channel direction for electrical transport than the zigzag direction. We further investigate the influence of nanoribbon width and channel thickness on the electrostatic control, conductivity, field-effect and intrinsic hole mobility. Finally, the hydrogen treatment is evaluated to effectively improve the hysteresis, reduce the interface states density (D_{it}), and improve the contact resistance

X. Feng, Dr. X. Huang, L. Chen, Dr. W. C. Tan, Dr. L. Wang, Prof. K.-W. Ang
Department of Electrical and Computer Engineering
National University of Singapore
4 Engineering Drive 3, Singapore 117583, Singapore
E-mail: eleakw@nus.edu.sg

X. Feng, Dr. X. Huang, L. Chen, Dr. W. C. Tan, Dr. L. Wang, Prof. K.-W. Ang
Centre for Advanced 2D Materials
National University of Singapore
6 Science Drive 2, Singapore 117543, Singapore

 The ORCID identification number(s) for the author(s) of this article can be found under <https://doi.org/10.1002/adfm.201801524>.

DOI: 10.1002/adfm.201801524

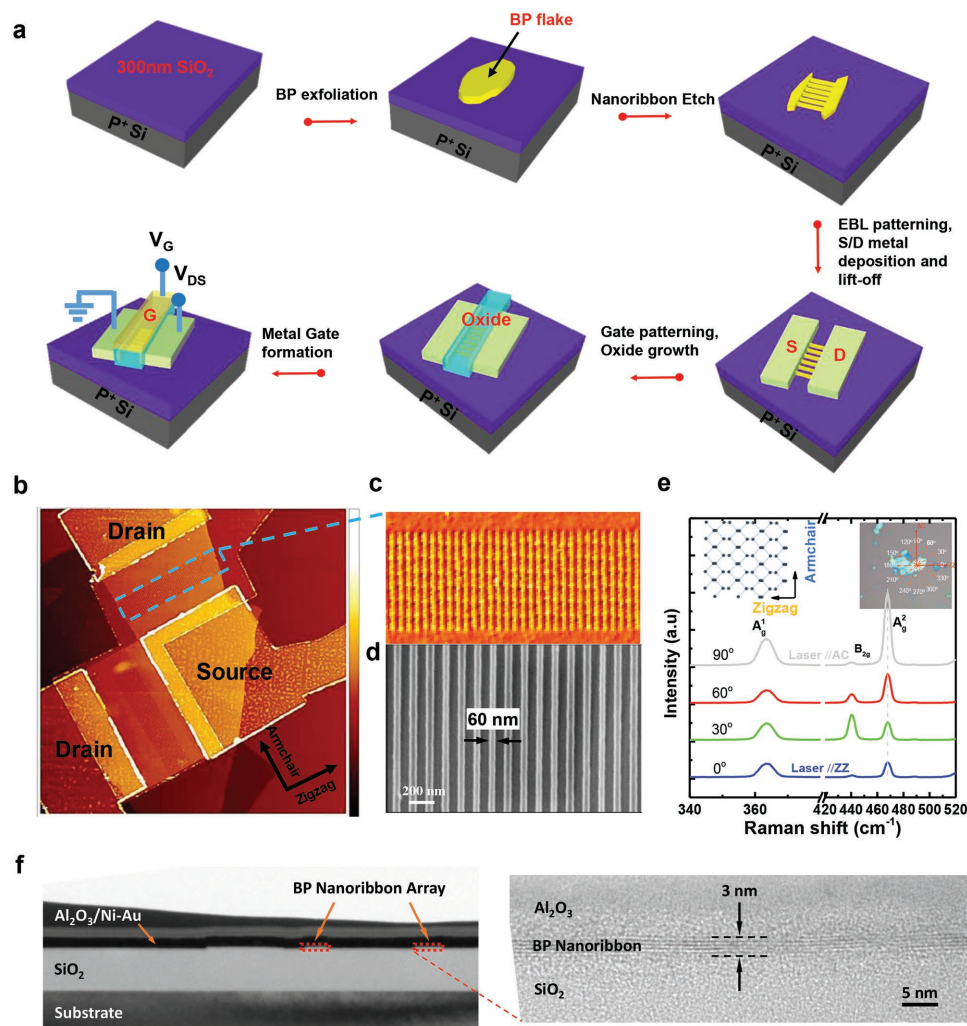


Figure 1. a) The fabrication flow of the black phosphorus nanoribbons field-effect transistor (BPNR-FET). A 20 nm ALD Al_2O_3 was grown at 120 °C as the top gate dielectric. b) Atomic force microscope (AFM) image of the BPNR-FET along the armchair (AC) and zigzag (ZZ) orientations together with the S/D electrodes and metal gate. An array of 60 nm wide nanoribbons is successfully formed. c) An enlarged AFM picture of the nanoribbons array. d) SEM image showing the precise measurement of nanoribbon width of 60 nm. e) Polarized Raman spectra of BP flakes (inset). The AC and ZZ orientations are determined by the variation of B_{2g} and A_g^2 phonon modes. f) High-resolution transmission electron microscopy (HRTEM) image showing the BP nanoribbons array, with a thin BP thickness of ≈ 3 nm.

simultaneously. This work demonstrates the potential of BPNR-FET as a high-performance p-type transistor in addition to the nanoribbon FET family which includes not only graphene and transition metal dichalcogenides (TMDs), but also group-IV, III–V compounds, and some heterojunctions.

2. Results and Discussion

2.1. Fabrication of BPNR-FET

Figure 1a illustrates the fabrication flow for realizing BP nanoribbons field-effect transistor at low process temperatures. BP films were mechanically exfoliated onto SiO_2 (300 nm)/Si substrate. Angle-resolved polarized Raman spectroscopy was performed to determine the crystallographic orientation. E-beam lithography (EBL) was then employed to pattern the

designated nanoribbons along armchair and zigzag crystal direction, respectively. After that, the exposed area was totally etched away by applying CHF_3/O_2 plasma to avoid the formation of source/drain (S/D) leakage path. S/D was then patterned using EBL and followed by 3/40 nm Ni/Au deposition using metal sputtering system. A 20 nm Al_2O_3 top gate dielectric was subsequently deposited by atomic layer deposition (ALD) to passivate the device. Finally, metal gate was sputtered with 3/40 nm Ni/Au. A detailed experiment process is described in the Experimental Section. **Figure 1b,c** shows the atomic force microscopy (AFM) image of the BP-nanoribbons FET along the armchair and zigzag direction together with the S/D electrodes and metal gate. A nanoribbon width of 60 nm is measured using scanning electron microscope (SEM) (**Figure 1d**). Polarized Raman spectra of the BP flake under different sample rotation angles are depicted in **Figure 1e**, which are collected using 532 nm laser excitation

under parallel-polarization configuration (the polarization of Raman scattered light is parallel to the incident light). Inset shows the optical image of the corresponding BP flake. The sample rotation angle is indicated by six arrowed lines separated by 30° . Three characteristic phonon peaks at 362 , 438 , and 466 cm^{-1} corresponding to A_g^1 , B_{2g} , and A_g^2 vibration modes are shown. It can be seen that B_{2g} mode intensity varies with a period of 90° and minimum intensity is found to be corresponding to either armchair or zigzag orientation. The direction could be further identified as the intensity of A_g^2 mode is typically strongest along the armchair direction.^[17,18,22,23] A cross-sectional high-resolution transmission electron microscopy (HRTEM) image (Figure 1f, left) is taken across the nanoribbon direction. The analysis further confirms that the crystallinity of

BP nanoribbons is preserved, showing no detrimental effects due to reactive ion etching (Figure 1f, right).

The BPNRs are patterned via a precisely controlled RIE method. To date, reactive ion gas such as Ar ,^[24] O_2 ,^[25] SF_6 ,^[26] and other methods like ozone treatment,^[27] reactive oxygen and water rinse,^[28] and laser treatment^[29] have been reported to control the BP thickness. In this work, CHF_3 with an added oxygen (O_2) component is employed as a feed gas for chemical downstream etching of BP nanoribbons. The evolution of optical microscope images as a function of plasma exposure time in Figure 2a clearly indicates the reduction of the flake thickness. The number of the remaining BP layers was accurately measured by AFM as plotted in Figure S1 (Supporting Information). The recipe achieves a constant etch rate of

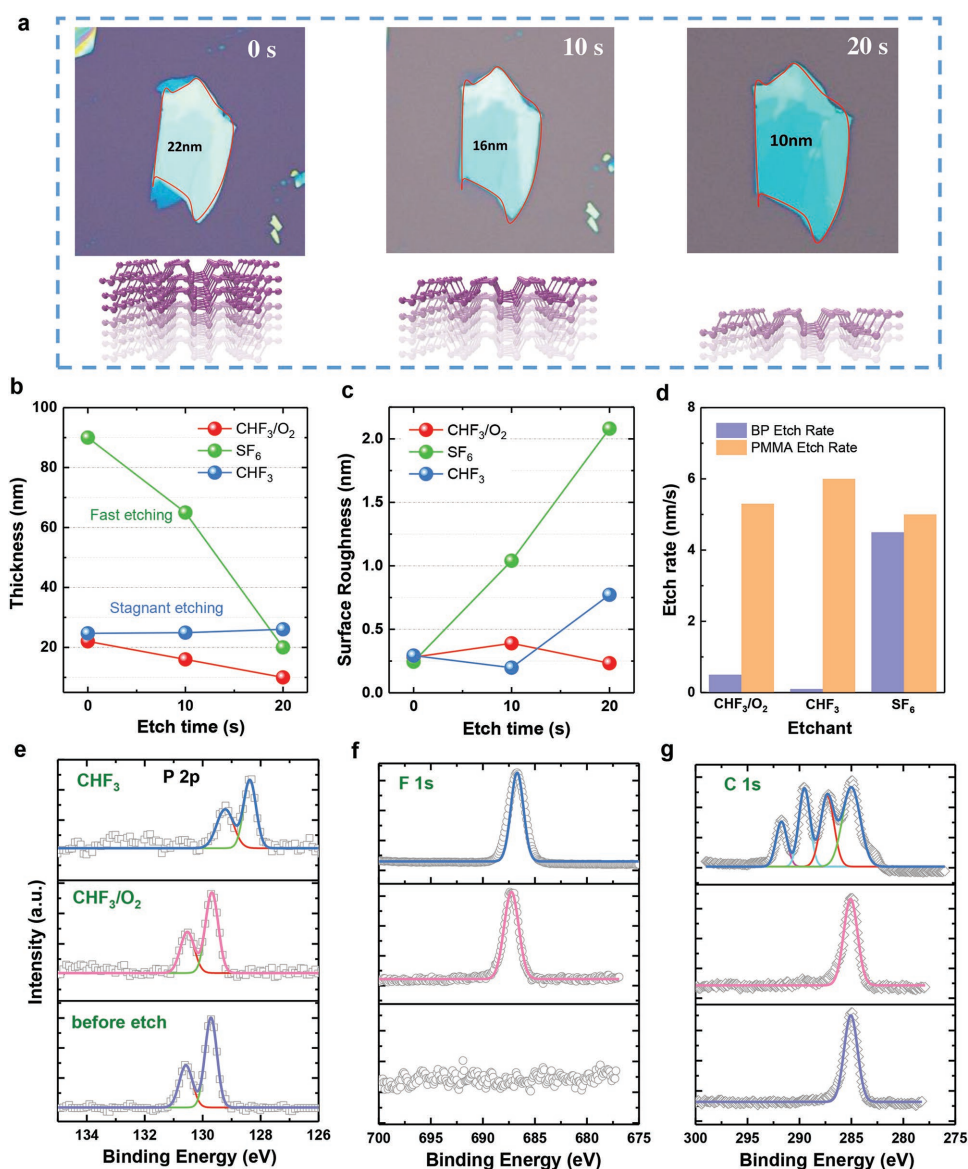


Figure 2. a) Optical images of the as-exfoliated BP flake, after 10 s CHF_3/O_2 plasma treatment and after 20 s CHF_3/O_2 plasma treatment, respectively. b) BP thickness and c) surface roughness as a function of etch time using different feed gases such as CHF_3/O_2 , pure CHF_3 , and SF_6 . d) Selectivity of BP over PMMA in different feed gases. PMMA was used as the soft mask. XPS spectra of e) P 2p, f) F 1s, and g) C 1s signals of the pristine BP before etch (bottom row), after CHF_3/O_2 plasma treatment (middle row) and after CHF_3 plasma treatment (top row).

0.6 nm s⁻¹. As the interlayer spacing of BP is ≈0.53 nm,^[5] a layer-by-layer thinning is expected. We also examined the etch conditions of other fluorine-based plasma gas such as SF₆ and pure CHF₃. The etch rate is shown to increase by several times in SF₆ plasma due to the intensive reaction with S and F (Figure 2b). Without the addition of O₂ in pure CHF₃ plasma, the etching process becomes stagnant. Hence, SF₆ and CHF₃ are deemed not the effective precursors for achieving atomic layer etching of black phosphorus. A further investigation of the surface morphology of BP films after plasma treatment is shown in Figure 2c. Starting with a fresh surface root mean square (RMS) of ≈0.25 nm, the BP surface remains clean and smooth after CHF₃/O₂ plasma treatment of 30 s. In addition to a precisely controlled thinning down rate, a good selectivity of BP over PMMA (1:5) is achieved (Figure 2d). Here, PMMA is used as the soft mask while the exposed part of BP is removed by plasma etching. The Raman spectra as shown in Figure S2 (Supporting Information) reveal that the pristine properties of BP are preserved after the plasma treatment.

We further examine the chemical bonding states of BP before and after plasma treatment by X-ray photoelectron spectroscopy (XPS). Figure 2e–g shows the XPS spectra of P 2p (panel 2e), F 1s (panel 2f), and C 1s (panel 2g) peaks of BP film before etch (bottom), after CHF₃/O₂ treatment (middle), and after pure CHF₃ plasma treatment (top). The single spin–orbit split doublet observed in the deconvolution of P 2p core level spectra at a binding energy of ≈130 eV denotes the intrinsic crystallinity of BP after the plasma treatment (panel 2e). The appearance of F 1s peak after plasma treatment indicates that fluorine radicals mainly react with phosphorus (panel 2f). Phosphorus halides like gaseous PF₃, PF₅, or PO₂F₂ by-products are assumed to be formed as their boiling point are low enough to be volatile at room temperature (see Section S3, Supporting Information).^[26] During oxygen-deficient discharges of pure CHF₃ plasma, a fluorocarbon layer is expected to form on the BP surface that inhibits the active species, F atoms, from reaching the BP surface. This is confirmed by the high carbon concentration in XPS (panel 2g, top) and ultraslow etch rate with pure CHF₃ gas (Figure 2b). The introduction of small amount of oxygen would suppress the formation of fluorocarbon layer and result in the formation of carbon monoxide (CO) gas phase which allows BP to be etched efficiently by F radicals. The nonappearance of P_xO_y peaks at ≈133 eV after plasma treatment indicates that this process differs from other etching techniques that utilize oxidation of BP.^[25] The absence of the pretreatment step to transform BP into phosphoric acid makes CHF₃/O₂ more favorable because of its clean and controllable properties.

2.2. Electrical Properties of BPNR-FET

To study the effect of width scaling on the BPNR-FET performance, we measure the transfer characteristic (I_d – V_g) of bulk and nanoribbons with different widths of 200, 150, and 60 nm along the armchair direction, as shown in Figure 3a. These devices are fabricated on a large 12 nm thick BP flake. The ON-state current density at $V_g = -6$ V and the subthreshold swing (SS) are summarized in Figure 3b. An increased ON-state current density from 0.6 to 2.4 μA μm⁻¹ and a sharp decrease in SS from 2.69 V dec⁻¹ to 563 mV dec⁻¹ are clearly

observed when the channel width is reduced from bulk (4 μm) to 60 nm wide nanoribbons. This implies that the top gate offers an efficacious electrostatic control in nanoribbons which accounts for the short channel effect improvement. In Figure 3c, we further investigate the orientation-dependent electrical performance by comparing the transfer curves along armchair and zigzag crystalline direction. The AFM image of this device is shown in Figure 1b with a BPNR thickness of 28 nm. The armchair-oriented BPNR-FET achieves a 3.2 times higher maximum current as compared with zigzag direction at a gate overdrive of –6 V. The linear output characteristic I_d – V_d in Figure 3d implies high-quality Ohmic-like contacts which has been formed between the metal electrodes and BPNR channel in strong hole accumulation regime. From the transfer characteristic of the BPNR-FET, we extract the field-effect mobility and intrinsic mobility as plotted in Figure 3e. The field-effect mobility is estimated using $\mu_{FE} = \frac{L}{W} \frac{1}{C_{ox}} \frac{dG}{d(V_g - V_{th})}$,

where L and W are the length and width of the BPNR channel, respectively, and C_{ox} is the capacitance per unit area. Hole field-effect mobilities of 394 cm² V⁻¹ s⁻¹ along the armchair direction and 144 cm² V⁻¹ s⁻¹ along the zigzag direction are achieved. To decouple the effect of contact resistance, we extract the intrinsic mobility by $\mu_0 = \mu_{FE} \frac{L}{L + \mu_{FE} W C_{ox} R_{sd}}$.^[30] A high

intrinsic peak mobility of 703 and 242 cm² V⁻¹ s⁻¹ along the armchair and zigzag directions is clearly seen. This confirms that the superior hole transport properties along the armchair orientation because of a lighter hole effective mass of 0.15 m_0 than the zigzag direction (1.54 m_0).^[31] Figure S3 (Supporting Information) presents an anisotropic bulk BP-FET with the same channel thickness of 28 nm to make a direct comparison with BPNR-FET (see Section S4, Supporting Information for details). The field-effect mobility of bulk BP-FET along the AC direction is extracted to be ≈70 cm² V⁻¹ s⁻¹, which is comparable to previously reported value in top-gated transistor with Al₂O₃ gate dielectric,^[32] but is six times smaller than the mobility seen in BPNR-FET. We further compute the conductivity σ which is calculated from the relationship between carrier concentration and mobility, that is, $\sigma = n_i q \mu_{FE}$, as shown in Figure 3f. The carrier concentration is estimated based on parallel-capacitor model^[33] (see Section S5, Supporting Information). The conductivity of BPNR is shown to increase by almost an order of magnitude higher than the bulk BP. We believe that the improved channel conductivity is primarily due to an improved electrostatic gate control. Inset in Figure 3f shows the schematic drawing of the top- and sidewall-gated BPNRs. Here, the effective width W_{eff} is increased to $W + 2h$ (h is the thickness of BP films), thus the conduction channel is adequately gated which effectively removes the influence of interlayer resistance and charge screening effect typically seen in bulk BP-FET.^[2,3] This has led to an improved channel conductivity and the achievement of a high hole mobility up to 703 cm² V⁻¹ s⁻¹ in a 28 nm thick BPNR-FET.

We further explore the BP thickness dependence which is mostly based on the armchair direction due to its better performance. Figure 4a shows three representative transfer characteristics of BPNR-FET with different channel thickness ranging from 4 to 28 nm. For a 4 nm thick BPNR, the on/off current ratio is increased to ≈10³ and a field-effect mobility

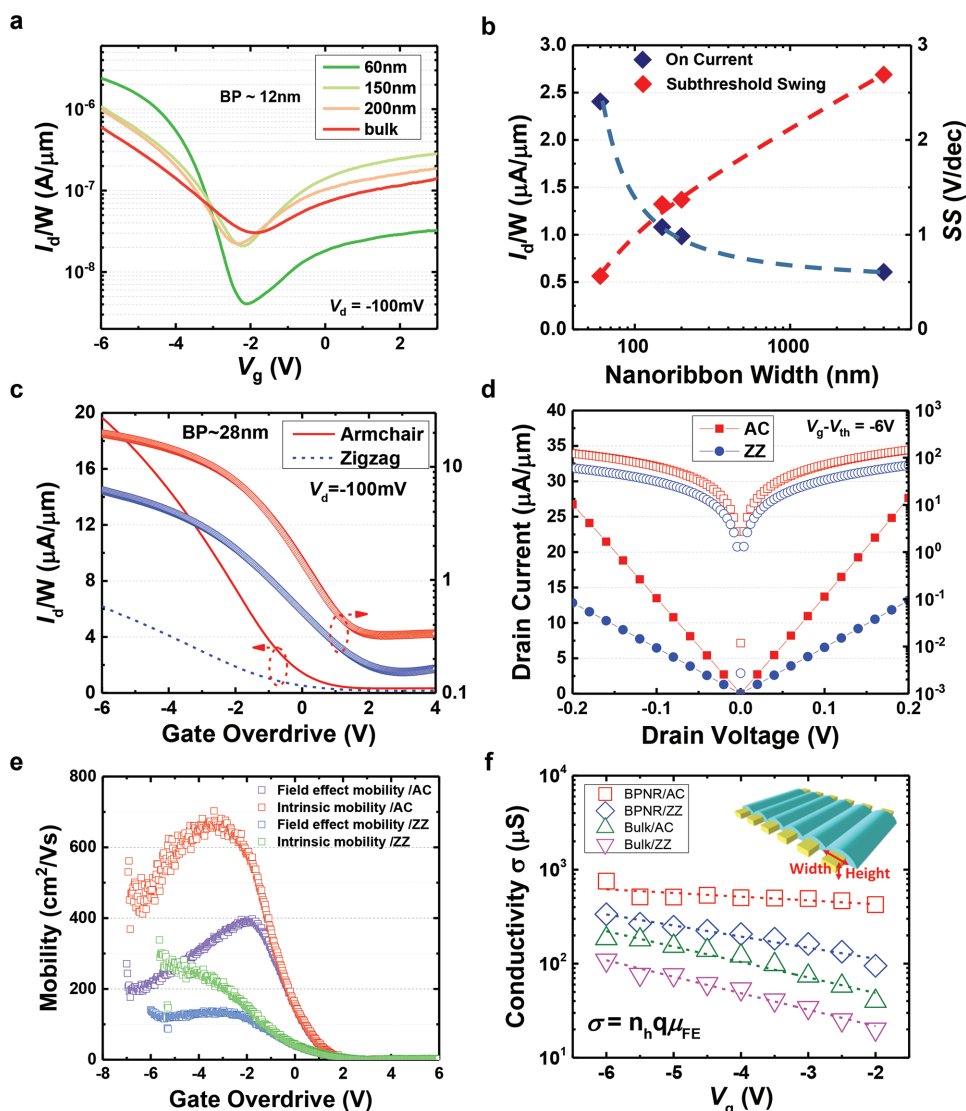


Figure 3. a) I_d - V_g curves for a bulk BP-FET and BPNR-FET with width of 200, 150, and 60 nm, respectively. The devices are fabricated together in one large 12 nm thick BP flake. b) The on-state current at $V_g = -6$ V and SS of four devices mentioned in (a). c) The I_d - V_g curves and d) the output characteristic I_d - V_d curves of a 28 nm thick, 60 nm wide, and 2 μ m long BPNR-FET with transport direction along the armchair (red) and zigzag (blue) orientations. e) The field-effect and intrinsic mobility of BPNR-FET versus gate overdrive. The FE mobility is computed to be 394 $\text{cm}^2 \text{V}^{-1} \text{s}^{-1}$ (AC) and 144 $\text{cm}^2 \text{V}^{-1} \text{s}^{-1}$ (ZZ), respectively. The hole peak intrinsic mobility is 703 $\text{cm}^2 \text{V}^{-1} \text{s}^{-1}$ (AC) and 242 $\text{cm}^2 \text{V}^{-1} \text{s}^{-1}$ (ZZ). f) The calculated conductivity σ as a function of gate voltage V_g for the 28 nm thick BPNR-FET and bulk BP-FET described in Figure S3 (Supporting Information). An increase in effective width corresponding to nanoribbon width (w) and height (h), that is, $w + 2^z h$, is schematically shown in the inset.

of 145 $\text{cm}^2 \text{V}^{-1} \text{s}^{-1}$ is achieved. The transconductance peak in Figure 4b increases from 0.62 to 1.24 $\mu\text{S} \mu\text{m}^{-1}$ and further to 3.95 $\mu\text{S} \mu\text{m}^{-1}$ for a $V_d = -100$ mV as the thickness is increased from 4 to 28 nm, implying an increasing trend of hole mobility. Figure 4c plots the nonmonotonic variation of the intrinsic hole mobility as a function of channel thickness along the armchair and zigzag orientations. Two competing phenomena would account for the observed trend. First, as the BP flake is thinned to sub-5 nm, the charge impurity at the BP/SiO₂ interface causes the mobility to decrease. This explains the increasing trend in hole mobility as the thicker BPNRs are less susceptible to the influence of charge impurities at the BPNR/SiO₂ interface. Second, the edge defects play a detrimental role as the

BP thickness is increased further. This is because thick BPNR suffers from longer etch time and is expected to have much more edge defects. Hence, more of its carriers is being scattered and thus its mobility would start to decrease. Figure 4d benchmarks the state-of-the-art research on nanoribbon formed using different materials, synthesis techniques, and electrical performance (see Section S5, Supporting Information). We summarize some prominent work on nanoribbon field-effect transistor including p-type graphene nanoribbon,^[13,14] n-type transition metal dichalcogenides (TMDs) such as MoS₂,^[34] CdSe,^[35] CdS,^[36] tri-chalcogenides TiS₃,^[37] III-V compound like boron nitride,^[38] and even superlattice such as AlGaIn/GaN heterojunctions.^[39] Compared with graphene nanoribbon,

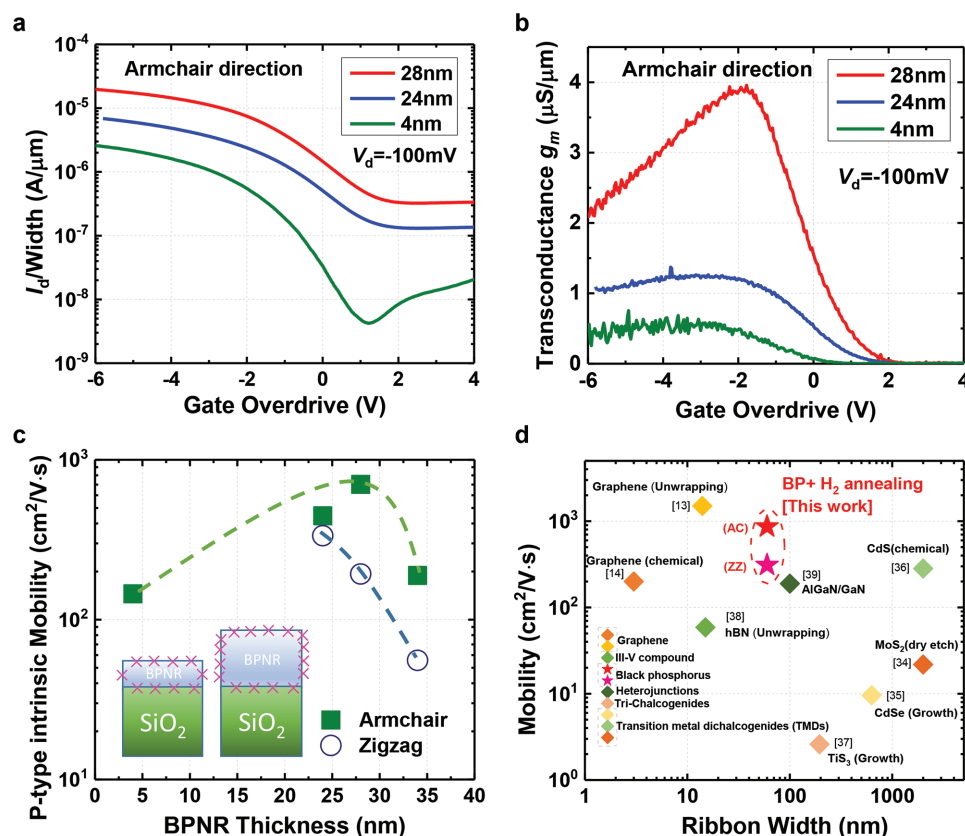


Figure 4. a) Transfer curve, I_d - V_g of the BPNR-FET with different channel thicknesses of 4, 24, and 28 nm. A nanoribbon width of 60 nm is patterned along the armchair direction. b) The corresponding transconductance curve of the devices in panel (a). The increasing trend of g_m indicates enhanced carrier mobility as the thickness increases. c) The p-type intrinsic mobility as a function of BPNR thickness. The nonmonotonic variation of mobility implies different scattering mechanism as shown in the inset of panel (c). The green and blue lines are drawn as an eye guide to show the mobility trend versus BPNR thickness. d) The mobility versus nanoribbon width of BPNR-FET in this work and the comparison to reference values reported in the literature. The nanoribbon width in ref.^[14] is 1.5–3.5 nm, here we use an average value of 2.5 nm as the representation. A detailed description of the synthesis technique and electronic behavior is listed in Table S2 (Supporting Information).

the BPNR-FET achieves a high hole mobility at the same time simplifies the fabrication complexity needed to open up the bandgap in graphene. The mobility of $862 \text{ cm}^2 \text{ V}^{-1} \text{ s}^{-1}$ (AC) and $310 \text{ cm}^2 \text{ V}^{-1} \text{ s}^{-1}$ (ZZ) shown in Figure 4d is based on the 28 nm thick device after hydrogen anneal to improve the interface properties.

2.3. Interface Engineering via Hydrogen Treatment

Hydrogenation has been an effective interface engineering technique to passivate the possible dangling bonds. The BPNR-FET was annealed in a vacuum furnace at 200 °C for 20 min under forming gas ambient with a mixture of 5% hydrogen and 95% Ar. Figure 5a,b shows the transfer curves of BPNR-FET along the armchair and zigzag crystal directions before and after hydrogen treatment. The hysteresis, ΔV_T , is defined as the gate voltage difference corresponding to a specific current density when the gate bias is swept in two opposite directions. Apparently, the as-fabricated device shows a larger hysteresis with ΔV_T of 1.28 and 2.78 V along the armchair and zigzag directions, respectively. The V_{th} -instability is believed to be attributed to charge traps/impurities located at the BPNR/high- κ

gate dielectric and metal/BP interfaces.^[40] The forming gas annealing (FGA) treatment largely reduces the charge traps in both interfaces, resulting in a smaller hysteresis of 0.83 and 0.85 V for AC- and ZZ-direction, respectively. The hysteresis is observed to be comparable to bulk BP-FET featuring Al_2O_3 gate dielectric and scandium (Sc) contact.^[41] This implies the effectiveness of FGA in removing the moisture at interface and healing the defects induced by dry etch. We further examine

the interface state density D_{it} as calculated using $D_{it} = \frac{C_{ox}\Delta V_T}{q}$.

When subjected to hydrogen treatment, it is observed that the D_{it} along AC and ZZ directions is decreased by 35 and 69%, respectively, as shown in Figure 5c. The consequential reduction in D_{it} confirms the effectiveness of hydrogen in passivating the dangling bonds at the interface. A quantitative analysis of the contact resistance between BP and S/D metal is further conducted. We extract and plot the contact resistance before and after FGA in Figure 5d. The total resistance in a field-effect transistor is the summation of channel resistance ($R_{channel}$) and S/D resistance ($2R_c$). At infinitely negative V_g , the total resistance would reduce to $2R_c$ as the channel resistance becomes negligible due to high inversion carrier density. A polynomial curve is used to fit the

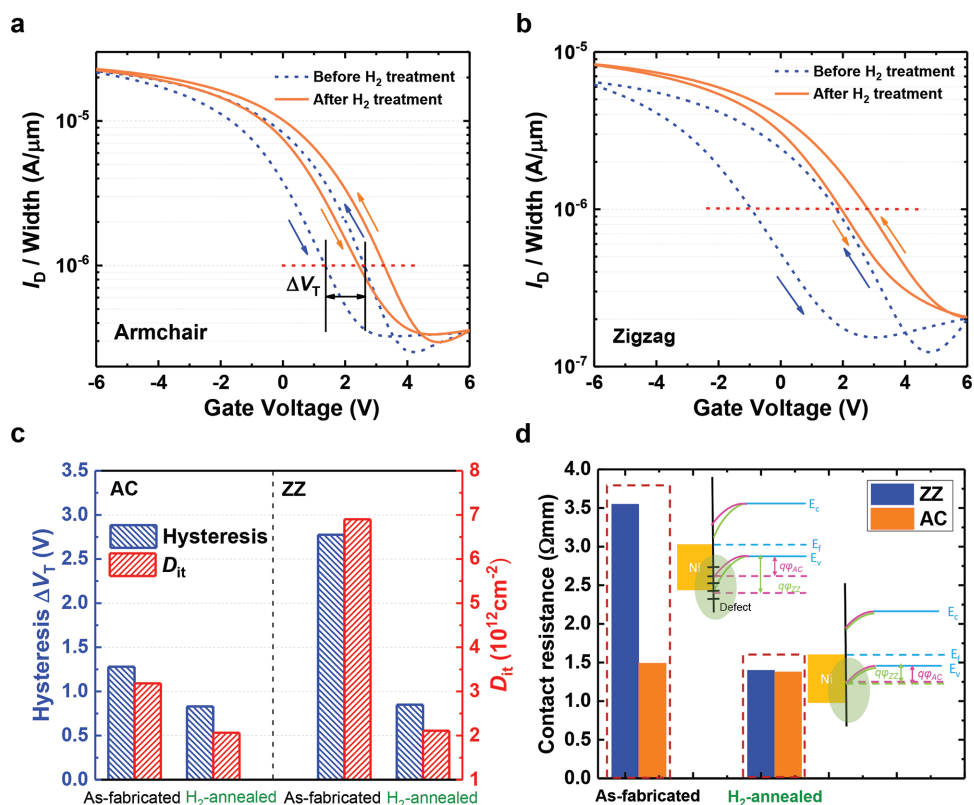


Figure 5. Transfer characteristic of BPNR-FET with transport channel along a) armchair and b) zigzag direction. The blue and yellow lines represent the current density of the as-fabricated device and after H₂ annealing at 200 °C for 20 min. c) Hysteresis (blue) and corresponding trap density D_{it} (red) extract from panels (a) and (b). The hysteresis, ΔV_T , is defined as the gate voltage difference corresponding to a current density of 10^{-6} A μm^{-1} during the forward and backward V_g sweeps. d) The contact resistance extracted from BPNR-FET before and after H₂ anneal. Insets are the schematic plots showing the Fermi-level pinning and depinning effect.

total resistance versus gate voltage V_g curve in which the total resistance plateaus off to reach $2R_c$ at infinite V_g .^[42] A representative methodology to extract the contact resistance is shown in Section S7 (Supporting Information). The contact resistance difference with relation to the as-fabricated BP device is attributed to the different Fermi-level pinning at the metal/BP interface. It is worthy to note that the Schottky barrier height (SBH) at the zigzag-oriented interface is higher due to a stronger Fermi level pinning by the interface defects, as schematically illustrated in Figure 5d inset. Fortunately, the Fermi level pinning could be modulated by annealing in forming gas ambient. After the hydrogen treatment, the contact resistance at ZZ interface reduces from 3.59 to 1.48 Ω mm, which approaches the AC-oriented contact resistance of 1.38 Ω mm. Moreover, this value is comparable to bulk BP-FET with palladium (Pd) contact (1.05 Ω mm) after Pd–H alloy formation^[43] and even smaller than previously reported thermally evaporated Ni contact resistance of 3.15 and 3.73 Ω mm.^[44,45] By physically sputtering the S/D area and treating the Ni contact with forming gas, the Ni contact resistance has been reduced to a record low value.

3. Conclusion

In summary, we have realized a first-of-its-kind black phosphorus nanoribbon field-effect transistor and conducted a

systematic study to investigate its performance dependence on crystal orientation, nanoribbon width, and channel thickness. BPNR-FET with 60 nm ribbon width has been demonstrated via a layer-by-layer dry etching technique. The adoption of 3D device structure effectively improves the electrostatic gate control over the channel, leading to a high hole mobility of 862 $\text{cm}^2 \text{V}^{-1} \text{s}^{-1}$ at room temperature. Moreover, hydrogenation anneal effectively improves the hysteresis, reduces the contact resistance down to 1.38 Ω mm, and simultaneously enhances the hole mobility. This work provides a pathway toward the development of nonplanar 2D devices based on BP nanoribbons and methods for further performance enhancement.

4. Experimental Section

Device Fabrication: Few-layer black phosphorus was mechanically exfoliated from a bulk BP crystal (purity 99.998%, Smart Element) and then transferred onto a 300 nm SiO₂ substrate. The exfoliation was performed inside an argon-filled glove box with O₂ and H₂O concentration <1 ppm. After the exfoliation, the sample was immediately spin-coated with PMMA (495, A4) used as soft mask with a rotation speed of 4000 rpm for 70 s. Optical microscope was then used to quickly find the flakes of interest. A nanoribbons array with 60 nm width was patterned by Jeol EBL (JBX-6300FS). The exposed areas were etched away by deep reactive ion etching (Oxford Plasma Pro100). The sample was then bathed in acetone for few hours during which, PMMA will be lifted

off from the sample, leaving the BP nanoribbons only. The source/drain was patterned with EBL again and Au/Ni (40 nm/3 nm) metals were deposited by sputtering (AJA ATC-2200 UHV Sputter). After the second lift-off process, the wafer was quickly transferred into the atomic layer deposition (Savannah ALD) chamber and Al₂O₃ gate dielectric (20 nm) was grown on the device at a low substrate temperature of 120 °C with TMA (pulsed at 15 ms) and water (pulsed at 15 ms) as the precursors. The process took 200 cycles (≈4 h) of pulsing and purging of TMA and water. Before unloading the sample, the ALD chamber is increased to 200 °C and subsequently cooled to room temperature. This step lasted ≈1 h to thermally anneal the sample which would promote the formation of Ni₂P alloy. The top gate was finally formed with Au/Ni (40 nm/3 nm) metals deposition by sputtering. The sample was then bathed in acetone for the third time to lift off the unwanted metals.

Reactive Ion Etching: The reactive ion etching process was developed using Oxford Plasma Pro Cobra 100 Deep RIE system. The dry etch was performed at 40 W with a 45/5 sccm CHF₃/O₂ flow rate.

XPS: Core level spectra were collected using a monochromatic Al K α X-ray source ($h\nu = 1486.69$ eV). The binding energies of all spectra were referenced to C1s which is set to 285 eV.

Supporting Information

Supporting Information is available from the Wiley Online Library or from the author.

Acknowledgements

This research was supported by the A*STAR Science and Engineering Research Council Grant (No. 152-70-00013), and by the National Research Foundation, Prime Minister's Office, Singapore, under its medium-sized center program.

Conflict of Interest

The authors declare no conflict of interest.

Keywords

anisotropy, black phosphorus, nanoribbons, phosphorene, transistors

Received: February 28, 2018

Revised: April 9, 2018

Published online: May 21, 2018

- [1] P. Bridgman, *J. Am. Chem. Soc.* **1914**, 36, 1344.
 [2] L. Li, Y. Yu, G. J. Ye, Q. Ge, X. Ou, H. Wu, D. Feng, X. H. Chen, Y. Zhang, *Nat. Nanotechnol.* **2014**, 9, 372.
 [3] W. C. Tan, Y. Cai, R. J. Ng, L. Huang, X. Feng, G. Zhang, Y.-W. Zhang, C. A. Nijhuis, X. Liu, K.-W. Ang, *Adv. Mater.* **2017**, 26, 1700503.
 [4] G. Long, D. Maryenko, J. Shen, S. Xu, J. Hou, Z. Wu, W. K. Wong, T. Han, J. Lin, Y. Cai, R. Lortz, N. Wang, *Nano Lett.* **2016**, 16, 7768.
 [5] X. Ling, H. Wang, S. Huang, F. Xia, M. S. Dresselhaus, *Proc. Natl. Acad. Sci. USA* **2015**, 112, 4523.
 [6] A. Prakash, Y. Cai, G. Zhang, Y.-W. Zhang, K.-W. Ang, *Small* **2017**, 13, 1602909.
 [7] H. Liu, A. T. Neal, Z. Zhu, Z. Luo, X. Xu, D. Tománek, P. D. Ye, *ACS Nano* **2014**, 8, 4033.
 [8] M. Buscema, D. J. Groenendijk, S. I. Blanter, G. A. Steele, H. S. Van Der Zant, A. Castellanos-Gomez, *Nano Lett.* **2014**, 14, 3347.
 [9] a) L. Huang, W. C. Tan, L. Wang, B. Dong, C. Lee, K.-W. Ang, *ACS Appl. Mater. Interfaces* **2017**, 9, 36130; b) W. C. Tan, L. Huang, R. J. Ng, L. Wang, D. M. N. Hasan, T. J. Duffin, K. S. Kumar, C. A. Nijhuis, C. Lee, K.-W. Ang, *Adv. Mater.* **2018**, 30, 1705039.
 [10] C. Chen, N. Youngblood, R. Peng, D. Yoo, D. A. Mohr, T. W. Johnson, S.-H. Oh, M. Li, *Nano Lett.* **2017**, 17, 985.
 [11] Y. Li, E. C. Moy, A. A. Murthy, S. Hao, J. D. Cain, E. D. Hanson, J. G. DiStefano, W. H. Chae, Q. Li, C. Wolverton, X. Chen, V. P. Dravid, *Adv. Funct. Mater.* **2018**, 28, 1704863.
 [12] M. Freitag, T. Low, W. Zhu, H. Yan, F. Xia, P. Avouris, *Nat. Commun.* **2013**, 4, 1951.
 [13] L. Jiao, X. Wang, G. Diankov, H. Wang, H. Dai, *Nat. Nanotechnol.* **2010**, 5, 321.
 [14] X. Wang, Y. Ouyang, X. Li, H. Wang, J. Guo, H. Dai, *Phys. Rev. Lett.* **2008**, 100, 206803.
 [15] J. Xiao, M. Long, X. Zhang, D. Zhang, H. Xu, K. S. Chan, *J. Phys. Chem. Lett.* **2015**, 6, 4141.
 [16] V. Tran, L. Yang, *Phys. Rev. B* **2014**, 89, 245407.
 [17] X. Wang, A. M. Jones, K. L. Seyler, V. Tran, Y. Jia, H. Zhao, H. Wang, L. Yang, X. Xu, F. Xia, *Nat. Nanotechnol.* **2015**, 10, 517.
 [18] F. Xia, H. Wang, Y. Jia, *Nat. Commun.* **2014**, 5, 4458.
 [19] S. Lee, F. Yang, J. Suh, S. Yang, Y. Lee, G. Li, H. S. Choe, A. Suslu, Y. Chen, C. Ko, J. Park, K. Liu, J. Li, K. Hippalgaonkar, J. J. Urban, S. Tongay, J. Wu, *Nat. Commun.* **2015**, 6, 8573.
 [20] Z. Liu, K. Aydin, *Nano Lett.* **2016**, 16, 3457.
 [21] P. M. Das, G. Danda, A. Cupo, W. M. Parkin, L. Liang, N. Kharche, X. Ling, S. Huang, M. S. Dresselhaus, V. Meunier, M. Drndić, *ACS Nano* **2016**, 10, 5687.
 [22] X. Ling, S. Huang, E. H. Hasdeo, L. Liang, W. M. Parkin, Y. Tsumi, A. R. Nugraha, A. A. Puzos, P. M. Das, B. G. Sumpter, *Nano Lett.* **2016**, 16, 2260.
 [23] J. Wu, N. Mao, L. Xie, H. Xu, J. Zhang, *Angew. Chem., Int. Ed.* **2015**, 54, 2366.
 [24] J. Jia, S. K. Jang, S. Lai, J. Xu, Y. J. Choi, J.-H. Park, S. Lee, *ACS Nano* **2015**, 9, 8729.
 [25] J. Pei, X. Gai, J. Yang, X. Wang, Z. Yu, D.-Y. Choi, B. Luther-Davies, Y. Lu, *Nat. Commun.* **2016**, 7, 10450.
 [26] G. Lee, J.-Y. Lee, G.-H. Lee, J. Kim, *J. Mater. Chem. C* **2016**, 4, 6187.
 [27] S. Kim, Y. Jung, J.-Y. Lee, G.-H. Lee, J. Kim, *Nano Res.* **2016**, 9, 3056.
 [28] H. Kwon, S. W. Seo, T. G. Kim, E. S. Lee, P. T. Lanh, S. Yang, S. Ryu, J. W. Kim, *ACS Nano* **2016**, 10, 8723.
 [29] J. Lu, J. Wu, A. Carvalho, A. Ziletti, H. Liu, J. Tan, Y. Chen, A. Castro Neto, B. Özyilmaz, C. H. Sow, *ACS Nano* **2015**, 9, 10411.
 [30] K.-Y. Chan, E. Bunte, H. Stiebig, D. Knipp, *Phys. Rev. Lett.* **2006**, 89, 203509.
 [31] X. Han, H. M. Stewart, S. A. Shevlin, C. R. A. Catlow, Z. X. Guo, *Nano Lett.* **2014**, 14, 4607.
 [32] J. S. Kim, P. J. Jeon, J. Lee, K. Choi, H. S. Lee, Y. Cho, Y. T. Lee, D. K. Hwang, S. Im, *Nano Lett.* **2015**, 15, 5778.
 [33] B. Radisavljevic, A. Kis, *Nat. Mater.* **2013**, 12, 815.
 [34] H. Liu, J. Gu, P. D. Ye, *IEEE Electron Device Lett.* **2012**, 33, 1273.
 [35] J. S. Jie, W. J. Zhang, Y. Jiang, S. T. Lee, *Appl. Phys. Lett.* **2006**, 89, 133118.
 [36] X. Duan, C. Niu, V. Sahi, J. Chen, J. W. Parce, S. Emedocles, J. L. Goldman, *Nature* **2003**, 425, 274.
 [37] J. O. Island, M. Buscema, M. Barawi, J. M. Clamagirand, J. R. Ares, C. Sánchez, I. J. Ferrer, G. A. Steele, H. S. van der Zant, A. Castellanos-Gomez, *Adv. Opt. Mater.* **2014**, 2, 641.
 [38] H. Zeng, C. Zhi, Z. Zhang, X. Wei, X. Wang, W. Guo, Y. Bando, D. Golberg, *Nano Lett.* **2010**, 10, 5049.
 [39] S. Joglekar, M. Azize, E. J. Jones, D. Piedra, S. Gradecak, T. Palacios, *IEEE Trans. Electron Devices* **2016**, 63, 318.
 [40] a) Z.-P. Ling, J.-T. Zhu, X. Liu, K.-W. Ang, *Sci. Rep.* **2016**, 6, 26609; b) Z.-P. Ling, X. Feng, H. Jiang, Z. He, X. Liu, K.-W. Ang, in *2016 IEEE Silicon Nanoelectronics Workshop*, IEEE, Piscataway, NJ **2016**, pp. 24–25, <https://doi.org/10.1109/SNW.2016.7577967>.

- [41] L. Li, M. Engel, D. B. Farmer, S.-J. Han, H.-S. P. Wong, *ACS Nano* **2016**, *10*, 4672.
- [42] T. Roy, M. Tosun, J. S. Kang, A. B. Sachid, S. B. Desai, M. Hettick, C. C. Hu, A. Javey, *ACS Nano* **2014**, *8*, 6259.
- [43] Y. Ma, C. Shen, A. Zhang, L. Chen, Y. Liu, J. Chen, Q. Liu, Z. Li, M. R. Amer, T. Nilges, *ACS Nano* **2017**, *11*, 7126.
- [44] a) Z.-P. Ling, S. Sakar, S. Mathew, J.-T. Zhu, K. Gopinadhan, T. Venkatesan, K.-W. Ang, *Sci. Rep.* **2015**, *5*, 18000; b) Z.-P. Ling, K. Majumdar, S. Sarkar, S. Mathew, J.-T. Zhu, K. Gopinadhan, T. Venkatesan, K.-W. Ang, in *2016 Int. Symp. VLSI Technology, Systems and Application*, IEEE, Piscataway, NJ **2016**, <https://doi.org/10.1109/VLSI-TSA.2016.7480535>.
- [45] Y. Du, H. Liu, Y. Deng, P. D. Ye, *ACS Nano* **2014**, *8*, 10035.